Applied Physics A (2020) 126:889
https://doi.org/10.1007/s00339-020-04078-0

Applied Physics A
Materials Science & Processing

Cu–CuO and Cu–CuO–ZnO hybrid nanostructures as photocatalysts and catalysts for efficient removal of pollutants

Kavita Sahu[1] · Akhilesh Pandey[2] · Satyabrata Mohapatra[1]

Received: 14 June 2020 / Accepted: 14 October 2020 / Published online: 24 October 2020

Abstract
Cu–CuO and Cu–CuO–ZnO hybrid nanostructures were fabricated by wet chemical route. The structural and morphological properties of the synthesized nanomaterials were well characterized by Raman spectroscopy, X-ray diffraction, field emission scanning electron microscopy while their optical and photocatalytic parameters were studied by using UV–Vis absorption spectroscopy. The photocatalytic performance of Cu–CuO–ZnO hybrid nanostructures and Cu–CuO hybrid nanostructures were examined via photocatalytic decomposition of methylene blue and methyl orange dyes in water whereas catalytic properties of the synthesized hybrid nanostructures were examined through reductive transformation of 4-nitrophenol (4-NP) in water. The prepared nanostructures of Cu–CuO–ZnO completely decomposed methylene blue (MB) and methyl orange (MO) in 54 and 45 min, respectively while catalytic decay of 4-NP was achieved in just 2 min using Cu–CuO nanohybrids. The developed Cu–CuO and Cu–CuO–ZnO hybrid nanostructures are extremely capable for the practical and innovative photocatalytic decomposition of waste at large scale as well as catalytic reduction of toxic chemicals from wastewater.

Keywords Cu–CuO · Cu–CuO–ZnO · Hybrid nanostructures · Photocatalysts · Catalysts

1 Introduction

Metal oxide nanostructure frameworks have gained tremendous attention from research point of view as they find applications in gas sensors, solar cells, catalysis and photocatalysis [1–6]. Decomposition of effluents from wastewater in the presence of semiconductor photocatalysts has been an affluent interest in recent years. Wastewater from industries introduce a variety of hazardous organic and nitroaromatic compounds into water bodies. Among these, methylene blue (MB), methyl orange (MO) and 4-nitrophenol (4-NP) are the most common pollutants which pose serious threat to human health and hence their removal from wastewater is essential. CuO nanostructures are significantly used in catalytic and photocatalytic processes for the decomposition of harmful organic products [7–14]. Heterogeneous photocatalysts using CuO nanostructures supported with ZnO nanostructures can serve as efficient photocatalysts for the removal of organic effluents from wastewater since recombination rate of charge carriers reduces with the formation of heterojunctions between ZnO and CuO nanostructures which improves the activity. Hybrid nanostructures are effective to enhance the photocatalytic performance of photocatalysts [15–21]. Fabrication of hybrid nanostructures can be done by various methods including hydrothermal, microwave-assisted, electrodeposition, carbothermal, thermal decomposition and wet chemical route. Synthesis of hybrid nanostructures by wet chemical route is better than other methods due to low cost requirement and simplicity of the method [18, 22–24]. Photocatalytic degradation of rose bengal, MB and alizarin red S in the presence of nanocomposite of CuO and ZnO were investigated by Charbri et al. [25]. They reported rates of degradation of rose bengal, MB and alizarin red S to be 0.02318, 0.04663 and 0.01931 min^{-1}, respectively. Enhanced photocatalytic decomposition of acid red dye by CuO–ZnO nanohybrids was shown by Sathishkumar et al. [26]. In our earlier reported work, we have investigated the catalytic activities of different morphologies of CuO such as nanorods, nanosheets and flowers and the observed

✉ Satyabrata Mohapatra
smiuac@gmail.com

[1] University School of Basic and Applied Sciences, Guru Gobind Singh Indraprastha University, Dwarka, New Delhi 110078, India

[2] Solid State Physics Laboratory, Defense Research and Development Organization, Timarpur, Delhi 110054, India

rate constants for the reduction of 4-NP were found to be 0.1981 min^{-1}, 0.1074 min^{-1} and 0.5651 min^{-1}, respectively [27]. Catalytic reduction of 4-NP by hybrid nanostructures was also studied in an earlier work and observed that hybrid CuO/Cu_2O nanowires transformed 4-NP in just 4 min with rate constant of 0.501 min^{-1} [28]. Coupling of Cu with hybrid nanostructures improves the charge separation leading to further enrichment in the photocatalytic and catalytic activities of hybrid nanostructures. The main purpose of this study was to develop highly efficient catalysts and photocatalysts for the decomposition of pollutants in water. This study presents reusable Cu–CuO nanostructures and hybrid Cu–CuO–ZnO nanostructures synthesis for highly efficient catalytic and photocatalytic decomposition of harmful chemicals and organic effluents. Photocatalytic activities were demonstrated by using MB and MO dyes whereas their catalytic properties were studied by using 4-NP. Complete decomposition of MB and MO by the prepared Cu–CuO–ZnO nanohybrids were done in 54 and 45 min, respectively. Catalytic decomposition of 4-NP was done in just 2 min by Cu–CuO nanostructures.

2 Experimental

2.1 Materials and methods

Zinc acetate dihydrate, copper acetate hydrate and hydrazine hydrate were taken for synthesizing hybrid Cu–CuO–ZnO nanostructures. Copper acetate hydrate and zinc acetate dihydrate were obtained from Merck Germany while hydrazine hydrate ($N_2H_4{\cdot}H_2O$) was obtained from SRL India. MB, MO dyes and 4-NP were purchased from SRL India. Synthesis of hybrid Cu–CuO–ZnO nanostructures and Cu–CuO hybrid nanostructures was done by wet chemical approach. 50 mM of copper acetate and zinc acetate were dissolved in distilled water and precipitated with hydrazine hydrate at 90 °C under stirring for 3 h as shown in scheme 1. 2 mL

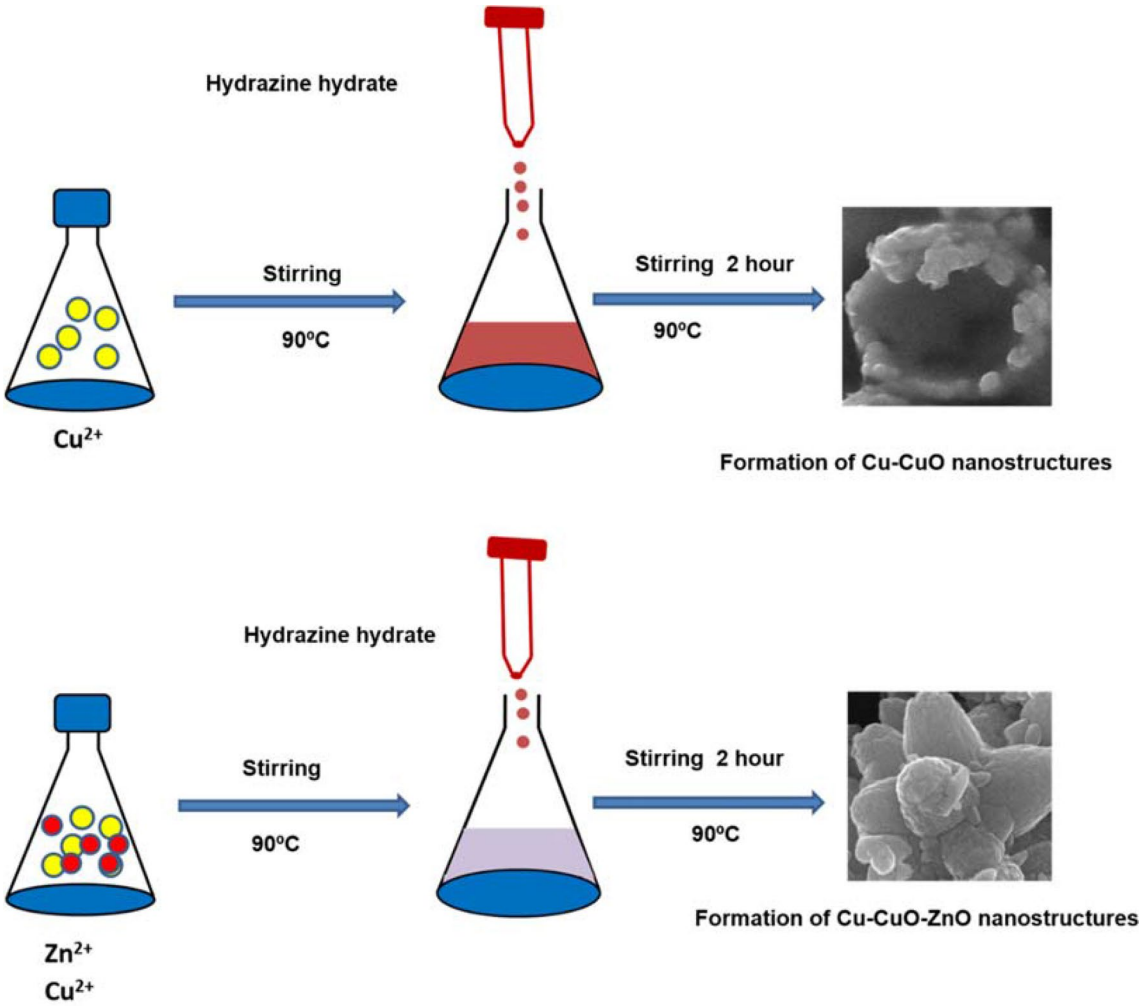

Scheme 1 Schematic of synthetic approach used

of hydrazine hydrate was added dropwise into the precursors solution. Cu–CuO hybrid nanostructures were also prepared by the above procedure but without using zinc acetate. Hybrid Cu–CuO and hybrid Cu–CuO–ZnO samples are referred as CH and CZH, respectively.

2.2 Photocatalytic measurements

The photocatalytic responses of as-synthesized Cu–CuO and Cu–CuO–ZnO hybrid nanostructures were determined by degrading MO (5 µM) and MB (5 µM) dyes under sunlight. 5 mg of as-synthesized samples were mixed in 5 µM of dye solutions. For equilibrium of adsorption and desorption on photocatalysts, mixtures were kept in dark for 20 min. The mixtures were left for different time intervals as 15, 30 and 45 min for MO dye whereas 14, 28, 42 and 56 min for MB dye under natural sunlight (~ 950 W/m^2) and all the photocatalytic experiments were done at 40 °C. UV–Vis spectroscopy was opted to explore the photocatalytic efficiency of as-synthesized Cu–CuO and hybrid Cu–CuO–ZnO nanostructures.

2.3 Radical species experiment

The role of radicals in the photocatalysis mechanism in prepared systems was investigated by using scavengers such as tertiary-butyl alcohol (TBA), formic acid (FA), benzoquinone (BQ) and cupric nitrate (CN) for the detection of hydroxyl radicals (·OH), holes (h^+), superoxide radicals ($\cdot O_2^-$) and electrons (e^-), respectively. Radical studies were carried out by dispersing as-synthesized samples into dye solutions with scavengers and finally exposed to sunlight.

2.4 Catalytic measurements

The catalytic performances of Cu–CuO and Cu–CuO–ZnO hybrid nanostructures were examined by reducing 4-NP into 4-AP. In catalytic process, 0.5 mL of the as-synthesized nanostructures (0.2 mg/mL) aqueous solution was mixed into 1 mL of aqueous $NaBH_4$ (5×10^{-2} M) and 1 mL of 4-NP (2.5×10^{-4} M). UV–Vis absorption spectra were checked to observe the catalytic efficiency of as-synthesized Cu–CuO and Cu–CuO–ZnO hybrid nanostructures for the transformation of 4-NP.

2.5 Characterizations

The morphological analyses of Cu–CuO and Cu–CuO–ZnO hybrid nanostructures were done using field emission scanning electron microscopy (FESEM) while Raman spectroscopy and X-ray diffraction (XRD) analyses were done to study the structural properties of the prepared nanostructures. XRD data were taken by using Panalytical X'pert Pro diffractometer (Cu K_α radiation of wavelength 0.1542 nm) while Raman spectra were recorded with Horiba Jobin Yvon LabRAM facility with Nd YAG laser (wavelength 532 nm). For PL measurements, 1 mg of the as-synthesized samples (CH and CZH) were mixed into 3 mL of ethanol in glass vials separately and PL spectra using Edinburgh Instruments with excitation wavelength of 325 nm (He-Cd laser) were recorded. Optical properties and photocatalytic activities were monitored with the help of UV–Vis absorption spectroscopy using HITACHI U-3300 dual beam spectrophotometer. For UV–Vis absorption measurements, 0.5 mg of as-synthesized samples (CH and CZH) were mixed into 3 mL of ethanol under sonication and absorption data were recorded by using HITACHI U-3300 dual beam spectrophotometer.

3 Results and discussion

Figure 1 shows the lower and higher magnification FESEM images of synthesized nanostructures in samples CH and CZH. Figure 1a, b displays the lower and higher magnification FESEM images of prepared nanostructures in sample CH. Formation of nanostructures was seen in sample CH. Figure 1c, d displays FESEM images of obtained nanostructures in sample CZH. Formation of hybrid nanostructures was observed in sample CZH. The average size of nanostructures in prepared samples CH and CZH were determined and found to be 714 and 320 nm, respectively. Figure 2 shows the typical Raman spectra of prepared nanostructures. Raman spectrum obtained from sample CH shows peaks at 278 and 609 cm^{-1} corresponding to the A_g and $B_g{}^2$ Raman modes of CuO, respectively while for sample CZH peaks at 266, 310, and 602 cm^{-1} are the A_g, $B_g{}^1$ and $B_g{}^2$ modes of CuO, respectively. In addition, two very small peaks were observed at 410 and 481 cm^{-1} which are ascribed to Cu_2O nanostructures [29], which usually form as the intermediates during hydrazine reduction. The spectrum shows peaks at 327, 432, and 661 cm^{-1} which are the $E_2{}^{(high)} - E_2{}^{(low)}$, $E_2{}^{(high)}$ and A_1 (LO) + $E_2{}^{(low)}$ modes of ZnO, respectively [30–34]. Structural properties of the as-synthesized nanostructures were analyzed by XRD technique as shown in Fig. 3. In sample CH, three diffraction peaks matched with (− 110), (200) and (112) planes of CuO (JCPDS 89-2529) and one peak matched with (111) planes of Cu (JCPDS 96-901-2044). In case of CZH sample, six peaks well matched with (100), (002), (101), (102), (110) and (103) planes of ZnO (89-1397) and one peak matched with the (112) plane of CuO (JCPDS 89-2529). In addition to these peaks, one peak matched with (111) planes of Cu (JCPDS 96-901-2044). The average crystallite size of nanostructures in samples CH and CZH were determined using Scherrer formula using a shape factor of 0.9 and found to be 14 and 12 nm, respectively. The presence of amorphous phase if any can be confirmed with

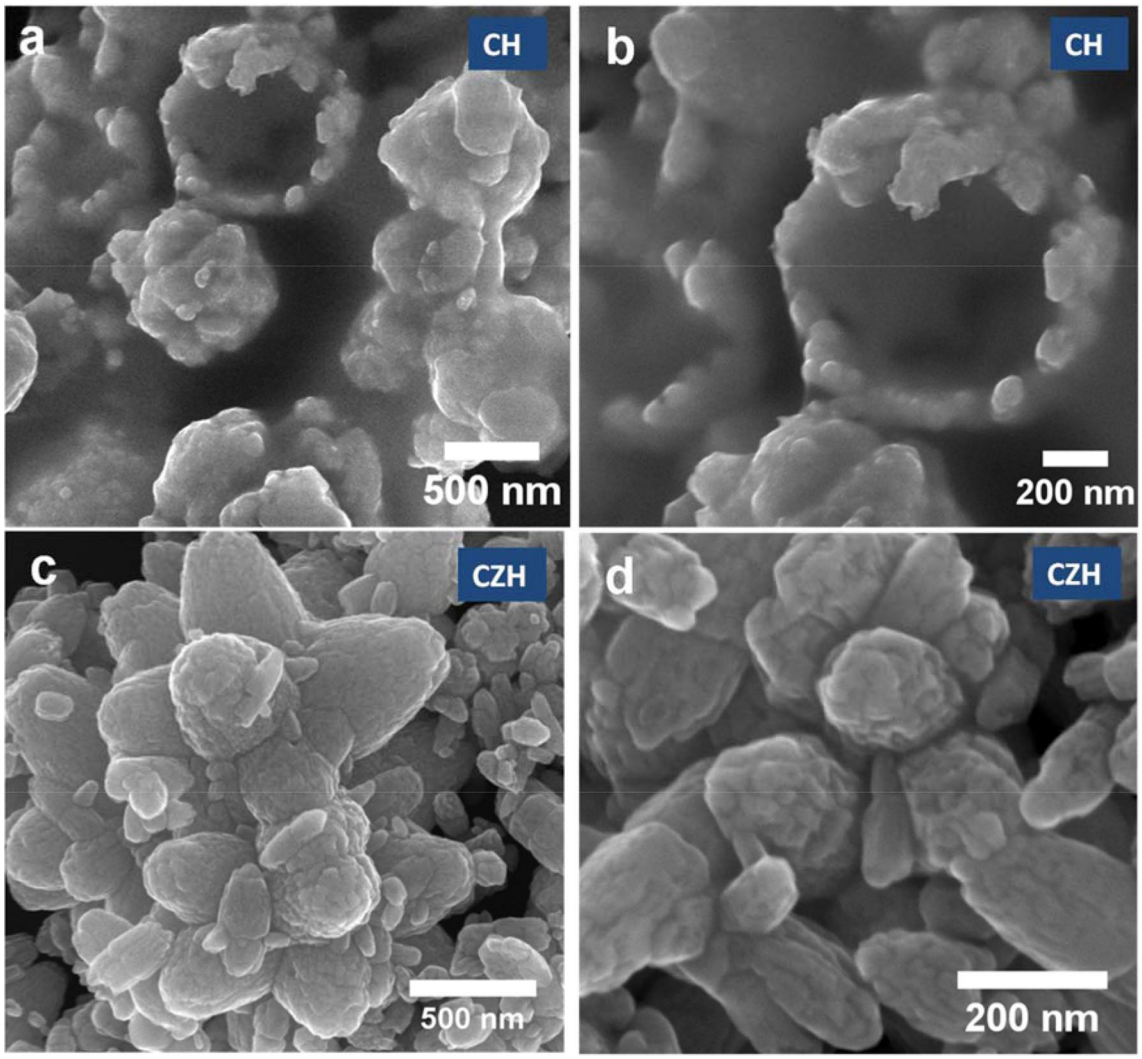

Fig. 1 **a**–**d** Lower and higher magnification FESEM mages of samples CH and CZH

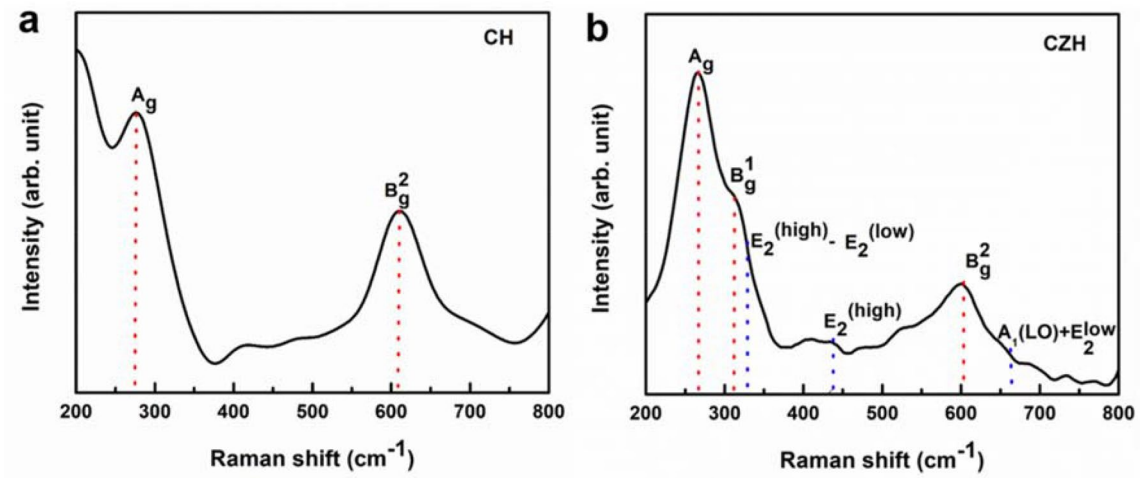

Fig. 2 Raman spectra of prepared nanostructures in samples CH and CZH

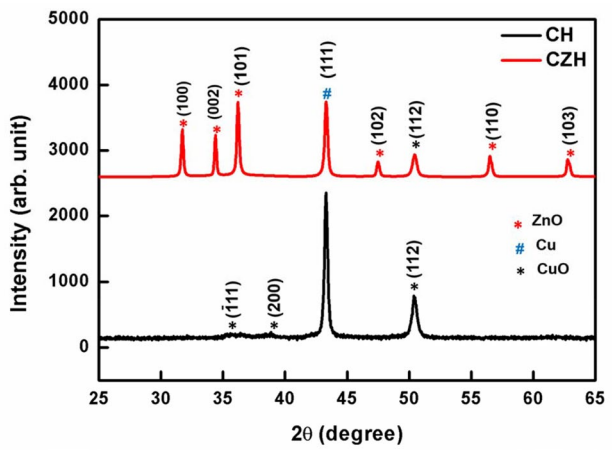

Fig. 3 XRD patterns of prepared nanostructures in samples CH and CZH

additional characterizations and can not be excluded based on our results. Raman and XRD data reveal Cu–CuO nanostructures in CH and hybrid Cu–CuO–ZnO nanostructures in CZH. It is important to note that no peaks corresponding Cu_2O were observed in the XRD patterns clearly indicating the very small fraction of Cu_2O which micro-Raman analysis could reveal due to its much higher sensitivity and/or its formation due to laser irradiation during Raman analysis. The formation of Cu–CuO and Cu–CuO–ZnO hybrid nanostructures can be understood in terms of hydrazine reduction of Cu^{2+} and Zn^{2+} ions and their hydroxides ($Cu(OH)_2$ and $Zn(OH)_2$) formed due to reactions with hydroxyl groups in the aqueous solution. In the presence of hydroxyl groups in the solution, Cu^{2+} and Zn^{2+} ions form nanosized precipitates of $Cu(OH)_2$ and $Zn(OH)_2$. In the hydrazine reduction process, each molecule of hydrazine (N_2H_4) gives four electrons, leaving behind protons and N_2 gas as byproducts [35]. These electrons reduce Cu^{2+} ions Cu^0 atoms forming Cu nanoparticles whereas $Cu(OH)_2$ nanostructures formed get reduced into Cu_2O which transform into CuO at 90 °C. $Zn(OH)_2$ nanostructures formed transform into ZnO at 90 °C and therefore hydrazine reduction of Cu and $Cu(OH)_2$ in the presence of $Zn(OH)_2$ leads to the formation of Cu–CuO–ZnO hybrid nanostructures.

Absorption spectra of samples CH and CZH were recorded to investigate their optical properties. Figure 4a displays the UV–Vis absorption spectra of obtained nanostructures. Absorption intensity was enhanced in case of Cu–CuO–ZnO nanostructures as compared to Cu–CuO. This enhancement in absorption provides the prospect for improving light utilization capability. Therefore, combination of ZnO with CuO can effectively enhance the light utilization capacity and can be used for enhancing photocatalytic activity. Photoluminescence spectra of prepared nanostructures are revealed in Fig. 4b. It is clearly noticed from PL spectra that photoluminescence intensity was enhanced in the case of hybrid Cu–CuO–ZnO nanostructures as compared to Cu–CuO nanostructures. Improved defect concentration in hybrid nanostructures of Cu–CuO–ZnO contribute to the enhancement in the visible emissions.

3.1 Photocatalytic studies

Photocatalytic activities for MB and MO dye decompositions by Cu–CuO and Cu–CuO–ZnO hybrid nanostructures were examined in the presence of sunlight. Figure 5a, b presents the temporal absorption spectra for degradation of MB dye by Cu–CuO and Cu–CuO–ZnO nanostructures, respectively. Significant decomposition of MB with the passage of time was observed. Figure 5c, d displays the variations in C/C_0 and ln C/C_0 for the obtained nanostructures, respectively. The results show that the efficiency for the

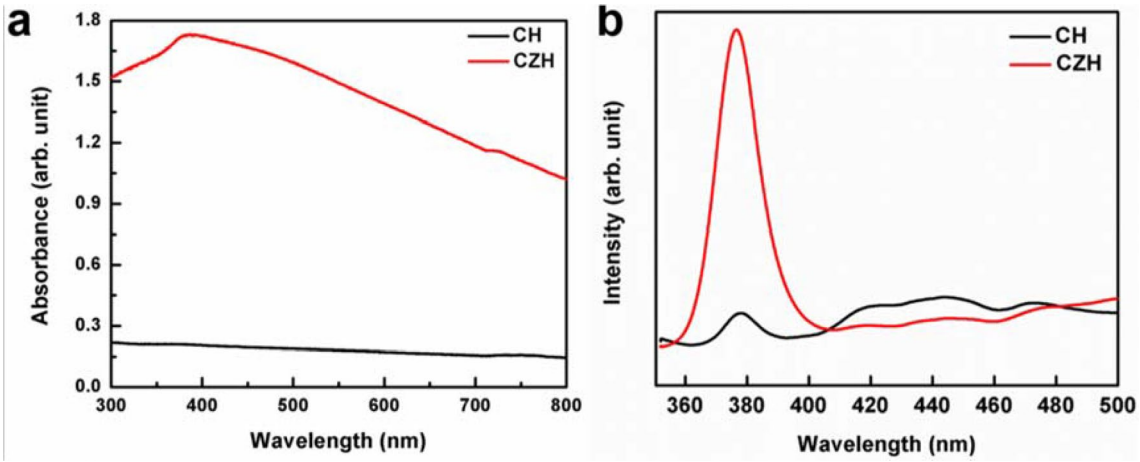

Fig. 4 **a** Absorption spectra of prepared nanostructures in samples CH and CZH, **b** photoluminescence spectra of prepared nanostructures

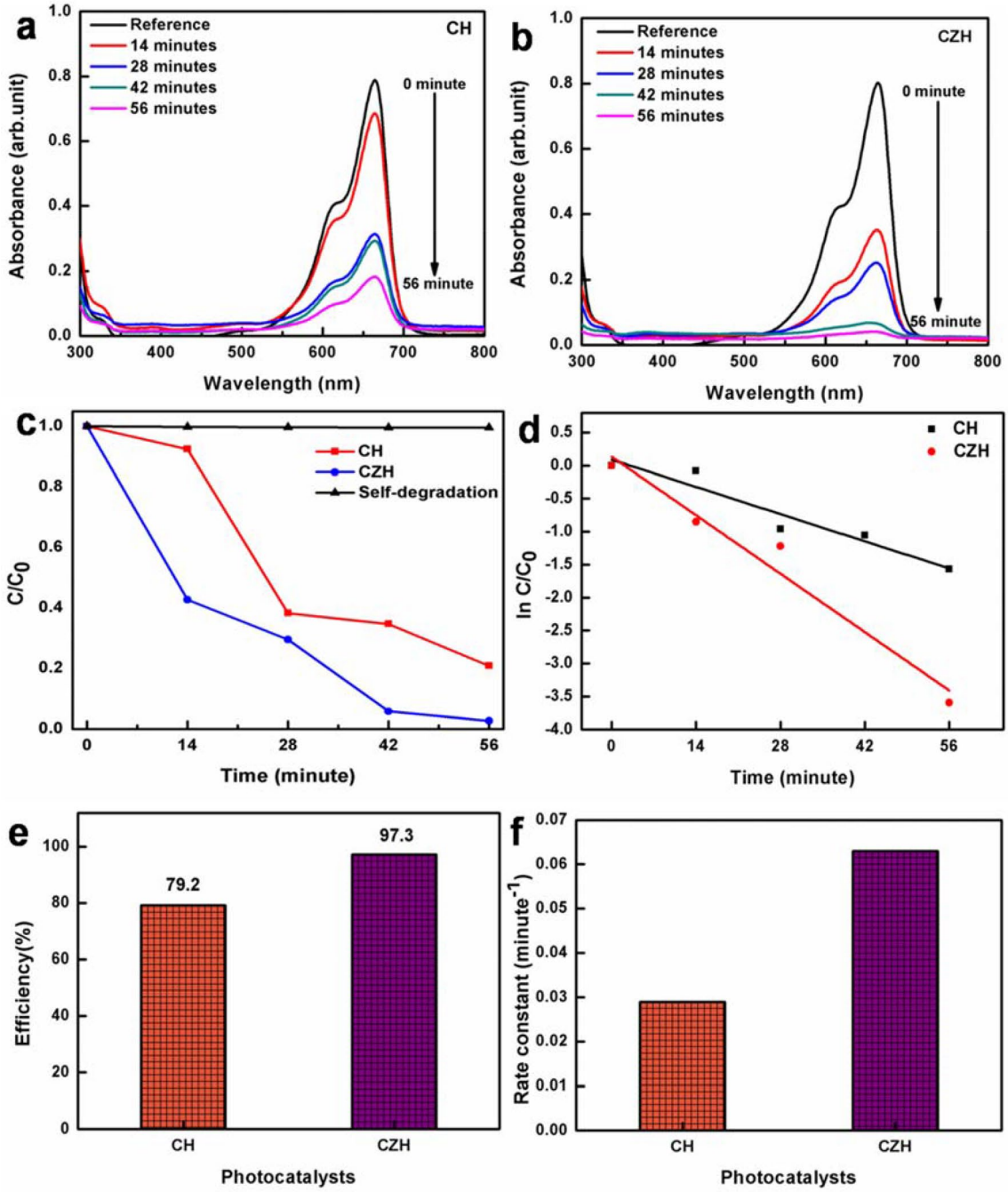

Fig. 5 **a**, **b** UV–Vis absorption of MB using photocatalysts CH and CZH, **c**, **d** C/C_0 and ln C/C_0 variation in the presence of CH and CZH, **e**, **f** Efficiency bar diagram and rate constants of synthesized nanostructures

decomposition of MB dye by Cu–CuO–ZnO nanostructures is higher than Cu–CuO nanostructures. Complete degradation of MB dye by Cu–CuO–ZnO nanostructures occurs in 56 min. Efficiency bar diagram and rate constants of synthesized nanostructures are displayed in Fig. 5e, f, respectively. As-synthesized Cu–CuO and Cu–CuO–ZnO nanostructures degraded 79.2% and 97.3% MB in 56 min, respectively. Rate constants of as-synthesized Cu–CuO and Cu–CuO–ZnO hybrid nanostructures were found to be 0.012 and 0.029 min^{-1}, respectively. Figure 6a, b presents the temporal absorption spectra for degradation of MO by Cu–CuO and Cu–CuO–ZnO nanostructures, respectively. Significant decomposition of MO with the passage of time was observed. Figure 6c, d displays variations in C/C_0 and ln C/C_0 for the obtained nanostructures, respectively. The results show that the efficiency for the removal of MO by

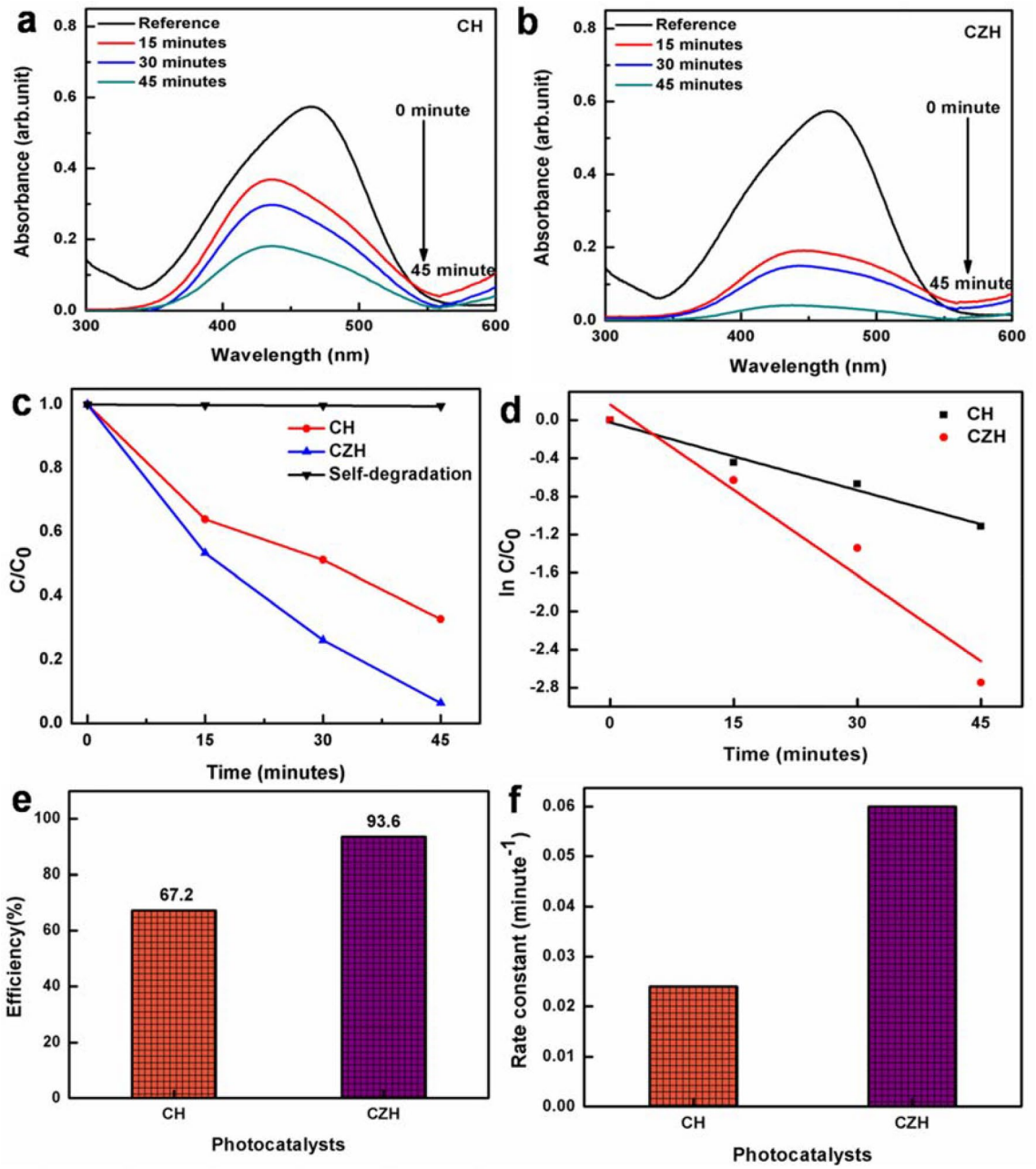

Fig. 6 **a**, **b** UV–Vis absorption of MO using photocatalyst CH and CZH, **c**, **d** C/C_0 and ln C/C_0 variation in the presence of CH and CZH, **e**, **f** Efficiency bar diagram and rate constants of synthesized nanostructures

Cu–CuO–ZnO hybrid nanostructures is higher than Cu–CuO nanostructures. Almost complete decomposition of MO dye by Cu–CuO–ZnO nanostructures occurred in 45 min. Efficiency bar diagram and rate constants of the synthesized hybrid nanostructures are displayed in Fig. 6e, f, respectively. As-synthesized Cu–CuO and Cu–CuO–ZnO nanostructures degraded 67.2% and 93.6% MO in 46 min, respectively. Rate constants of Cu–CuO and Cu–CuO–ZnO hybrid nanostructures were found to be 0.024 and 0.060 min^{-1}, respectively.

3.2 Photocatalytic mechanism

Probable photocatalytic decomposition mechanism in case of Cu–CuO and hybrid Cu–CuO–ZnO nanostructures can be understood with the help of schematic shown in Fig. 7. Upon irradiation of light on Cu–CuO nanostructures, generation of electrons and holes in the conduction and valence bands of ZnO and CuO system takes place independently. Photogenerated electrons migrate from CB of CuO to CB of ZnO while at the same time holes migrate from VB of

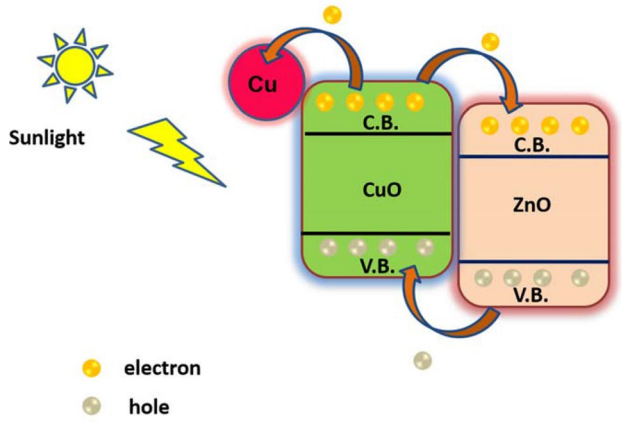

Fig. 7 Probable photocatalytic decomposition mechanism in prepared hybrid nanostructures

ZnO to VB of CuO. This direction of migration of electrons and holes in CuO–ZnO nanostructures take place since the lower energy level of CB of ZnO than CuO. Hydroxyl and superoxide radicals were produced upon contact of holes and electrons with water and oxygen, respectively. Decomposition of dye occurred due to the formation of hydroxyl and superoxide radicals. Presence of Cu nanostructures on CuO–ZnO system further slows down the recombination rate of charge carriers. This inhibits charge carrier recombination which leads to the enhanced efficiency of Cu–CuO–ZnO nanostructures. The effect of the radicals on the photocatalytic performance of Cu–CuO–ZnO hybrid nanomaterial was also examined since radicals play important role towards the degradation of dye. Figure 8 shows the efficiency bar diagram of Cu–CuO–ZnO nanostructures using scavengers. Photocatalytic efficiency decreased from 97.3 to 81.6% when BQ was added in the photocatalytic process. This signifies the minor role of superoxide radicals in dye degradation. When FA and CN were added into the mixture, efficiency was observed to 61.3% and 56.1%, respectively while upon addition of TBA drastic decrease in efficiency (from 97.3 to 28.5%) was observed. This drastic decrease in efficiency shows the major contribution of hydroxyl radicals in photocatalytic decomposition of dye. The role of ·OH radicals in the photocatalytic degradation of MB can be understood through their molecular level interactions [36–38]. First ·OH radicals attack the C–S^+=C functional group in MB leading to cleavage of bonds forming C–S(=O)–C and opening the aromatic ring at centre with S and N. The ·OH radical then interacts with the sulfoxide group twice forming sulfone and sulfonic acid in the process and finally releasing SO_4^{2-} ions upon subsequent reaction with ·OH radicals. In addition to the cleavage of bonds in the C–S^+=C functional group, cleavage of N=C double bond takes place. The photogenerated electrons reduce protons forming ·H radicals which lead to saturation of the two amino bonds. Upon substitution by an ·OH radical this amino group leads to formation of phenol along with release of ·NH_2 radical which produces ammonium ions and ammonia. The two symmetrical dimethyl-phenyl-amino groups degrade when ·OH radical reacts with the methyl group forming alcohol and then aldehyde which ultimately produces CO_2. The phenyl-methyl-amine radical is degraded by successive reactions with ·OH radicals resulting in the complete MB degradation.

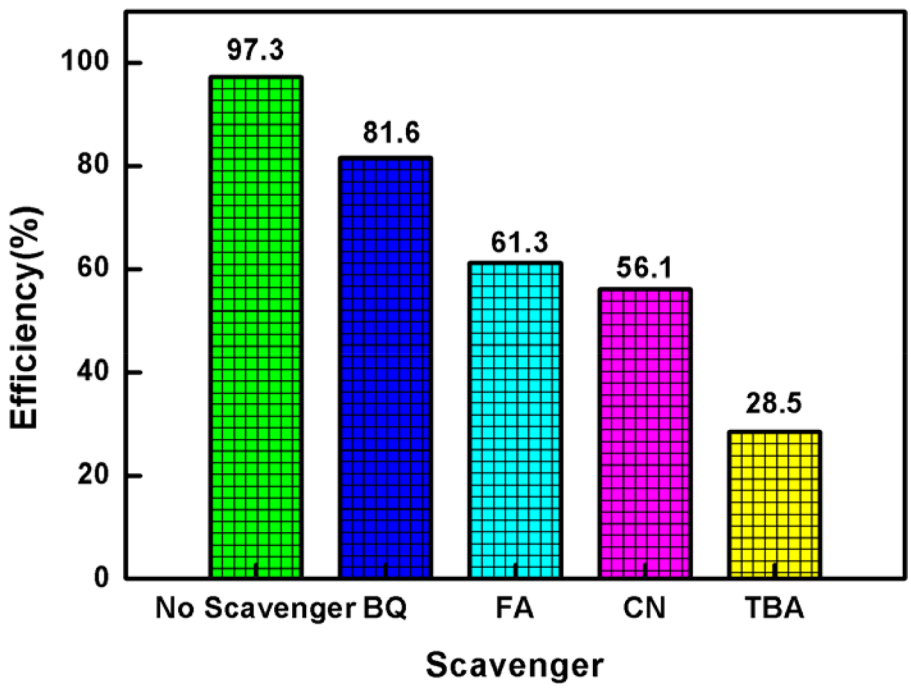

Fig. 8 Efficiency bar diagram of Cu–CuO–ZnO nanostructures with scavengers

3.3 Catalytic reduction of 4-nitrophenol

To explore the catalytic efficiency of the obtained Cu–CuO and Cu–CuO–ZnO hybrid nanostructures, reductive transformation of 4-NP to 4-AP in the presence of $NaBH_4$ was examined. Figure 9a, b shows the variation in the absorption spectra of 4-NP due to Cu–CuO and Cu–CuO–ZnO nanostructured catalysts, respectively. Characteristic peak of 4-NP (400 nm) significantly diminished whereas the new peak of 4-AP (300 nm) appeared. Figure 9c, d shows the C/C_0 and ln C/C_0 plots for the reduction of 4-NP by the synthesized catalysts. It can be visibly noticed that 4-NP reduction efficiency is more in case of Cu–CuO (CH) than Cu–CuO–ZnO nanostructures (CZH). Reduction of 4-NP was 95.6% and 67.5% in case of Cu–CuO and Cu–CuO–ZnO nanostructures, respectively as revealed in Fig. 9e. Rate constants were determined to be 0.74 and 0.28 min^{-1} for Cu–CuO and Cu–CuO–ZnO nanostructured hybrids, respectively (Fig. 9f). Photocatalytic and catalytic decomposition of dyes and 4-NP by prepared nanostructures has

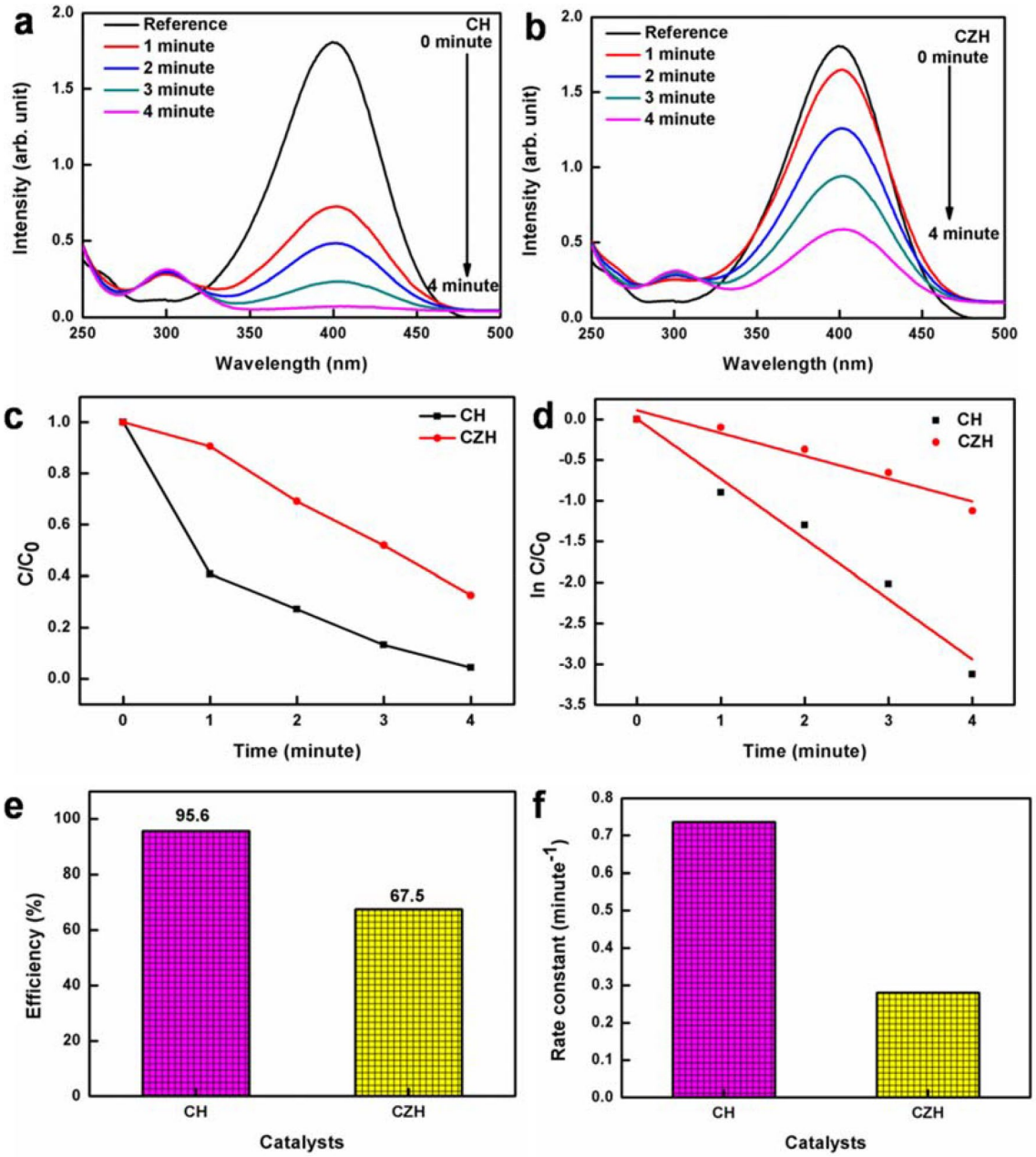

Fig. 9 Variation in absorption spectrum of 4-NP by catalysts **a** CH and **b** CZH, **c**, **d** C/C_0 and ln C/C_0 plots for the reduction of 4-NP by the synthesized catalysts, **e**, **f** efficiency and rate constants of synthesized structures

Table 1 Comparison of photocatalytic decomposition of dyes and catalytic reduction of 4-NP by prepared nanostructures with some of the literature work

Photocatalyst	Rate constant (min^{-1})	References
CuO–ZnO nanoparticles	0.086 (acid red dye)	[26]
CuO–ZnO nanocomposite	0.02318 (rose bengal)	[25]
CuO–ZnO nanocomposite	0.04663 (MB)	[25]
CuO–ZnO nanocomposite	0.01931 (alizarin red S)	[25]
Cu–CuO hybrid nanostructures	0.024 (MO)	This work
Cu–CuO–ZnO hybrid nanostructures	0.060 (MO)	This work
Cu–CuO hybrid nanostructures	0.029 (MB)	This work
Cu–CuO–ZnO hybrid nanostructures	0.063 (MB)	This work
Cu–CuO hybrid nanostructures	0.74 (4-NP)	This work
Cu–CuO–ZnO hybrid nanostructures	0.28 (4-NP)	This work

been compared with some of the literature work as shown in Table 1. The catalytic mechanism for reduction of 4-NP in water into 4-AP by the prepared samples CH and CZH involves three steps. In the first step, adsorption of 4-nitrophenolate ions on hybrid nanostructures in the samples CH and CZH takes place. Then electrons transfer from BH^{4-} ions to 4-NP is facilitated by the hybrid nanostructures contributing to 4-AP formation and finally desorption of 4-AP from hybrid nanostructures. Porous materials enhance the adsorption of 4-nitrophenolate anions on their surface leading to improved catalytic performance. In this work also, the prepared nanostructures of Cu–CuO sample CH has porous type nanostructures and display extremely high catalytic behaviour as compared to CZH due to better adsorption of 4-nitrophenolate anions.

Photocatalytic efficiency usually depends on parameters such as light utilization, crystal size, charge carriers' recombination, morphology and optical properties of the photocatalysts [39–41]. Combination of wide band gap and narrow band gap semiconductors enhances the utilization of light as well as inhibits the charge carriers' recombination which are important factors for improving the photocatalytic performance [42, 43]. Interface of ZnO and CuO leading to suppressed recombination consequently improved photocatalytic performance of nanocomposite of ZnO/Cu_2O for removal of textile dye was reported by Yu et al. [44]. In our case also, Cu–CuO–ZnO nanostructures showed higher activity than Cu–CuO nanostructures due to improvement in light utilization, smaller crystallite size and better suppression of recombination because of the nanoheterojunction of ZnO and CuO. Catalytic activity for the reducing 4-NP is highly reliant on the size, surface area and porosity of the catalysts [45, 46]. Porous materials enhance the adsorption of 4-nitrophenolate anions on their surface and the consequence is improvement in catalytic performance. Ag decorated RGO exhibited higher catalytic performance than pristine nanoparticles of Ag due to more surface area of Ag decorated RGO [47]. In this work also, the prepared nanostructures of Cu–CuO with porous type morphology display extremely high catalytic behavior due to better adsorption of 4-nitrophenolate anions as compared to Cu–CuO–ZnO nanostructures. In our work, sample CZH (Cu–CuO–ZnO nanostructures) shows improved photocatalytic activity than CH sample (Cu–CuO nanostructures) due to improved light utilization, smaller crystallite size and better suppression of charge recombination due to formation of heterojunctions between CuO and ZnO nanostructures. This work expresses a cost-effective easy route for the development of extremely effective reusable photocatalysts and catalysts for the decomposition of MB, MO and toxic 4-NP from waste water.

4 Conclusions

Cu–CuO–ZnO and Cu–CuO hybrid nanostructures were successfully fabricated by using wet chemical approach. The prepared hybrid Cu–CuO–ZnO nanostructures completely decomposed MB and MO in 54 and 45 min, respectively while catalytic decomposition of 4-NP was achieved in just 2 min using Cu–CuO nanohybrids. The improved photocatalytic efficiency in Cu–CuO–ZnO nanostructures as compared to Cu–CuO nanostructures is mostly due to the formation of nanoheterojunctions which consequently improved separation of charge carriers, smaller crystallite size and improvement in the light utilization capability. Apart from the significantly efficient photocatalytic activities, synthesized Cu–CuO and Cu–CuO–ZnO nanostructures also showed highly efficient catalytic performance for reducing 4-NP. The developed Cu–CuO and Cu–CuO–ZnO hybrid nanostructures are exciting for the practical and innovative photocatalytic decomposition of waste at large scale as well as catalytic reduction of toxic chemicals from waste water.

Acknowledgements KS thanks DST for funding in terms of DST-WOS-A (SR/WOSA-PM-10-2017(G&C)) project.

Compliance with ethical standards

Conflict of interest The authors declare that there is no conflict of interest regarding the publication of this paper.

References

1. S. Zaman, A. Zainelabdin, G. Amin, O. Nur, M. Willander, J. Phys. Chem. Solids **73**, 1320 (2012)
2. L. Saikia, D. Bhuyan, M. Saikia, B. Malakar, D.K. Dutta, P. Sengupta, Appl. Catal. A Gen. **490**, 42 (2015)

3. H. Xu, G. Zhu, D. Zheng, C. Xi, X. Xu, X. Shen, J. Colloid Interface Sci. **383**, 75 (2012)
4. K. Sahu, S. Kuriakose, J. Singh, B. Satpati, S. Mohapatra, J. Phys. Chem. Solids **121**, 186 (2018)
5. F. Han, V.S. Kambala, M. Srinivasan, D. Rajarathnam, R. Naidu, Appl. Catal. A Gen. **359**, 25 (2009)
6. S. Kuriakose, V. Choudhary, B. Satpati, S. Mohapatra, Phys. Chem. Chem. Phys. **16**, 17560 (2014)
7. X. Deng, C. Wang, M. Shao, X. Xu, J. Huang, RSC Adv. **7**, 4329 (2017)
8. K. Sahu, J. Singh, S. Mohapatra, J. Mater. Sci. Mater. Electron. **30**, 6088 (2019)
9. Q. Zhang, K. Zhang, D. Xu, G. Yang, H. Huang, F. Nie, C. Liu, S. Yang, Prog. Mater. Sci. **60**, 208 (2014)
10. K. Sahu, J. Singh, S. Mohapatra, Opt. Mater. **93**, 58 (2019)
11. A.A. Dubale, A.G. Tamirat, H.M. Chen, T.A. Berhe, C.J. Pan, W.N. Su, B.J. Hwang, J. Mater. Chem. A **4**, 2205 (2016)
12. K. Sahu, S. Choudhary, S.A. Khan, A. Pandey, S. Mohapatra, Nano-Struct. Nano-Obj. **17**, 92 (2019)
13. S. Kumar, C.M.A. Parlett, M.A. Isaacs, D.V. Jowett, R.E. Douthwaite, M.C.R. Cockett, A.F. Lee, Appl. Catal. B Environ. **189**, 226 (2016)
14. X. Liu, J. Chen, P. Liu, H. Zhang, G. Li, T. An, H. Zhao, Appl. Catal. A **521**, 34 (2016)
15. R. Sahay, J. Sundaramurthy, P.S. Kumar, V. Thavasi, S.G. Mhaisalkar, S. Ramakrishna, J. Solid State Chem. **186**, 261 (2012)
16. R. Saravanan, S. Karthikeyan, V.K. Gupta, G. Sekaran, V. Narayanan, A.J. Stephen, Mater. Sci. Eng. C **33**, 91 (2013)
17. A.E. Kandjani, Y.M. Sabri, S.R. Periasamy, N. Zohora, M.H. Amin, A. Nafady, S.K. Bhargava, Langmuir **31**, 10922 (2015)
18. K. Mageshwari, D. Nataraj, T. Pal, R. Sathyamoorthy, J. Park, J. Alloys Compd. **625**, 362 (2015)
19. B. Li, Y. Wang, Superlatt. Microstruct. **47**, 615 (2010)
20. W. Ang, X. Li, S. Li, L. Yan-Jun, L. Wei-Wei, Chin. Phys. Lett. **30**, 046202 (2013)
21. D. Malwal, P. Gopinath, Catal. Sci. Technol. **6**, 4458 (2016)
22. S. Kuriakose, D.K. Avasthi, S. Mohapatra, Beilstein J. Nanotechnol. **6**, 928 (2015)
23. T. Chang, Z. Li, G. Yun, Y. Jia, H. Yang, Nano-Micro Lett. **5**, 163 (2013)
24. O. Messaoudi, H. Makhlouf, A. Souissi, G. Amiri, A. Bardaoui, M. Oueslati, M. Bechelany, R. Chtourou, Appl. Surf. Sci. **343**, 148 (2015)
25. S. Chabri, A. Dhara, B. Show, D. Adak, A. Sinha, N. Mukherje, Catal. Sci. Technol. **6**, 3238 (2016)
26. P. Sathishkumar, R. Sweena, J.J. Wu, S. Anandan, Chem. Eng. J. **171**, 136 (2011)
27. K. Sahu, R. Singhal, S. Mohapatra, Catal. Lett. **150**, 471–481 (2020)
28. K. Sahu, B. Satpati, R. Singhal, S. Mohapatra, J. Phys. Chem. Solids **136**, 109143 (2020)
29. L.C. Chen, C.C. Chen, K.C. Liang, S.H. Chang, Z.L. Tseng, S.C. Yeh, C.T. Chen, W.T. Wu, C.G. Wu, Nanoscale Res. Lett. **11**, 402 (2016)
30. Y. Deng, A.D. Handoko, Y. Du, S. Xi, B.S. Yeo, ACS Catal. **6**, 2473 (2016)
31. T. Sander, C.T. Reindl, M. Giar, B. Eifert, M. Heinemann, C. Heiliger, P.J. Klar, Phys. Rev. B **90**, 045203 (2014)
32. J. Reydellet, M. Balkanski, D. Trivich, Phys. Status Solidi B **52**, 175 (1972)
33. X. Zhao, Y. Tan, F. Wu, H. Niu, Z. Tang, Y. Cai, J.P. Giesy, Sci. Total Environ. **571**, 380 (2016)
34. B. Cheng, W. Sun, J. Jiao, B. Tian, Y. Xiao, S. Lei, J. Raman Spectrosc. **41**, 1221 (2010)
35. X. Medvedeva, A. Vidyakina, F. Li, A. Mereshchenko, A. Klinkova, Nanomaterials **9**, 1445 (2019)
36. H. Gnaser, M.R. Savina, W.F. Calaway, C.E. Tripa, I.V. Veryovkin, M.J. Pellin, Int. J. Mass Spectrom. **245**, 61–67 (2005)
37. A. Houas, H. Lachheb, M. Ksibi, E. Elaloui, C. Guillard, J.M. Herrmann, Appl. Catal. B: Environ. **2001**(31), 145–157 (2001)
38. S. Kuriakose, B. Satpati, S. Mohapatra, Phys. Chem. Chem. Phys. **16**, 12741–12749 (2014)
39. B. Henkel, A. Vahl, O.C. Aktas, T. Strunskus, F. Faupel, Nanotechnol. **29**, 035703 (2017)
40. R. Nagaraja, N. Kottam, C.R. Girija, B.M. Nagabhushana, Powder Technol. **215**, 91 (2012)
41. S. Veziroglu, M.Z. Ghori, M. Kamp, L. Kienle, H.G. Rubahn, T. Strunskus, J. Fiutowski, J. Adam, F. Faupel, O.C. Aktas, A.C.S. Adv, Mater. Inter. **5**, 1800465 (2018)
42. Z. Jin, X. Zhang, Y. Li, S. Li, G. Lu, Catal. Commun. **8**, 1267 (2007)
43. D.L. Liao, C.A. Badour, B.Q. Liao, J. Photochem. Photobiol. A Chem. **194**, 11 (2008)
44. A. Bhattacharjee, M. Ahmaruzzaman, RSC Adv. **6**, 41348 (2016)
45. L. Chen, S. Shet, H. Tang, H. Wang, T. Deutsch, Y. Yan, J. Turner, M. Al-Jassim, J. Mater. Chem. **20**, 6962 (2010)
46. R. Al-Gaashani, S. Radiman, N. Tabet, A.R. Daud, J. Alloys Compd. **509**, 8761 (2011)
47. B. Vellaichamy, P. Periakaruppan, RSC Adv. **6**, 88837 (2016)